

Dielectric and Optical Spectroscopy of New Poly-Crystalline Ceramic for device Applications

Rajani K Parida

Siksha O Anusandhan University, ITER, Bhubaneswar

Sourav Bhattacharjee

Central Institute of Technology Kokrajhar

Bhagyashree Mohanty

Siksha O Anusandhan University, ITER, Bhubaneswar

Nimai C Nayak

Siksha O Anusandhan University, ITER, Bhubaneswar

Bichitra Nanda Parida (✉ bichitra72@gmail.com)

Central Institute of Technology Kokrajhar <https://orcid.org/0000-0002-7501-9377>

Original Research

Keywords: FTIR, UV-Visible, Dielectric, AC conductivity

Posted Date: February 15th, 2021

DOI: <https://doi.org/10.21203/rs.3.rs-196610/v1>

License:  This work is licensed under a Creative Commons Attribution 4.0 International License.

[Read Full License](#)

Version of Record: A version of this preprint was published at Journal of Materials Science: Materials in Electronics on April 26th, 2021. See the published version at <https://doi.org/10.1007/s10854-021-05932-4>.

Abstract

The polycrystalline double perovskite $\text{Li}_2\text{GdFeTiO}_6$ was synthesized through solid-state mixed oxide method and its preliminary crystal structure was investigated by XRD technique. The structure of the material was identified to be tetragonal with space group P4bm using POWD and MATCH software. The morphology of the sample was investigated through a scanning electron microscope (SEM) and the average grain size was found $3.82 \mu\text{m}$ using intercept technique. The investigation of the perovskite phase and various vibrational modes were carried out through FTIR spectroscopic technique. The band gap ($E_g = 1.73 \text{ eV}$) and visible light sensitivity of the material were identified by UV-Visible spectroscopic operation carried in the range 200–700 nm. The dielectric and related properties were investigated as a function of frequency and temperature using an impedance analyzer (LCR meter). Room temperature dielectric investigation suggests it may be useful for storage application. The transport activities investigated through conductivity, impedance and modulus technique illustrate the significant influence of grains on transportation of charges.

1. Introduction

Over the most recent couple of decades, multifunctional-multiferroic materials accumulate the attention of researchers working in the field of material science as a result of their fascinating physical properties, for example, ferromagnetic and ferroelectric includes at the same time in a single phase. These materials locate a wide scope of uses for devices, for example, piezoelectric sensors, photovoltaic/solar cells, arbitrary access memory, and many more [1, 2]. In this classification, perovskite materials are seen as a valuable and promising applicant. Perovskites are also found useful to improve the efficiency and performance of solid electrolytes. It is reported that lithium titanate based perovskites are a promising candidate for solid electrolytes because of its relatively high ionic conductivity and negligible electronic conductivity at room temperature [3–6]. In the framework of discovering new multifunctional material, we focus our attention towards Gadolinium (Gd)-based orthoferrites. In Gd-based orthoferrite, the exchange interaction $\text{Gd}^{3+} \leftrightarrow \text{Fe}^{3+}$ cause lattice distortion which triggers large electric polarization around anti-ferromagnetic Neel temperature [7, 8]. In the system of examination on material development, material specialists have figure out some derivates of perovskite. Among the derivatives, double perovskite oxide (DPO) with general recipe $\text{A}_2\text{BB}'\text{O}_6$ (where A = alkali/alkaline earth or rare-earth ion, B and B' = Transition metal ions and O = oxygen ion) has drawn the consideration of researchers due to their utilization as a cathode in moderate temperature solid oxide fuel cells. The accessibility of various distinct cations alongside oxygen anion in DPO widens their application for the device fabrication. Various theoretical and experimental investigations on DPO reveals that the different physical properties such as electrical, magnetic, optical etc. are very much influence by the size as well as the valence of the cations A, B and B'. Among the double perovskites, some members of the rare-earth family are found to exhibit very fascinating physical properties. The magnetic and transport investigation of $\text{La}_2\text{CoMnO}_6$ done by Sahoo et al. [9] reveals the existence of semiconducting features in the vicinity of ferromagnetic (FM) curie temperature. It is reported that on substitution of rare-earth (Sm and Gd) with small ionic radii at La-site

induce structural instability and destroy the long-range FM ordering [10]. It is also reported that $\text{La}_2\text{CoMnO}_6$ and $\text{Sm}_2\text{CoMnO}_6$ system possesses two FM transition while $\text{Gd}_2\text{CoMnO}_6$ has only one FM transition [9]. The double perovskite $\text{Lu}_2\text{CoMnO}_6$ shows magnetically tunable electric polarization due to breaking of spiral inversion symmetry [11]. The double perovskite system A_2NiMnO_6 (where A = La, Lu) exhibit polar behavior associated with lattice frustration due to variation of ionic radii of rare-earth site ion [12]. Filho et al. reported the spin-phonon coupling in Y_2NiMnO_6 due to expansion/contraction of the octahedral NiO_6 and MnO_6 [13]. Because of these fascinating and wide range spectra, we have focused our attention towards rare-earth to develop double perovskite with further improve properties. The double perovskites material can be obtained by combining two perovskite structures in proper stoichiometry. Based on this, we have synthesized double perovskite $\text{Li}_2\text{GdFeTiO}_6$ by combining the elements of gadolinium ferrite and lithium titanate in a suitable ratio. In this work, we have reported the structural, optical, dielectric and transport properties of $\text{Li}_2\text{GdFeTiO}_6$ in detailed.

2. Experimental Technique

The investigated sample was synthesized through solid-state route method by taking the raw chemicals Li_2CO_3 , Gd_2O_3 , TiO_2 and Fe_2O_3 in proper stoichiometry ratio. The proportionality of the raw chemicals was estimated by the following relation:



The raw chemicals were gently grounded in Agate Mortar and Pestle for 1–2 hours. After dry grounding of the raw chemicals, liquid methanol (CH_3OH) was added in it and again reground for duration of another 1–2 hours. The grounded powder sample was then put in an alumina crucible and placed in a furnace for calcination. After repeated firing technique, finally, a hard lump of the sample was found to form at 825°C which was consider as calcinations temperature. The lump sample was then broken and converted into homogeneous calcined powder using Agate Mortar and Pestle. For microstructure and electrical characterization, some portion of the calcined powder was pelletized into a circular disc of suitable dimension by exerting pressure through hydraulic press of the order 10^6 N/m . To improve the strength of the pellet sample polyvinyl alcohol (PVA) was added as a binder in the calcined powder before pelletization. Finally, pellet sample was sintered at around 875°C .

The room temperature XRD technique was incorporated for preliminary investigation of structure. The XRD was conducted on the calcined powder using X-ray diffractometer with CuK_{α} as incident radiation in the Bragg's angle (2θ) range $20^{\circ} \leq 2\theta \leq 80^{\circ}$ at a scanning rate $2^{\circ}/\text{min}$. The scanning electron microscope (SEM) (Model: JOEL JSM 5800) was incorporated for investigation of surface morphology of the pellet sample at room temperature. Investigation on different modes of vibration, functional group, etc. was done through FTIR spectroscopic technique using JASCO-FTIR/4100 infrared spectrometer. SHIMADZU-2600 UV-Visible spectrometer was incorporated for the investigation of optical properties in the range 200–700 nm. The dielectric and electric operations were conduct on the electrode pellet sample

by LCR meter (Model: PSM-1735, LCR N4L, UK) in the frequency and temperature range 1 kHz- 5 MHz and 25⁰C-525⁰C respectively.

3. Results And Discussion

3.1. Structural investigation:

The preliminary room temperature structural investigation was carried out in the diffraction angle (2θ) ranging from 20⁰- 80⁰ using X-ray diffraction (XRD) technique and depicted in Fig. 1. The observed sharp and unique peaks in the XRD profile differ from raw chemical suggest new structure has formed. The structural identification was done by utilizing standard programming software "POWD". In this technique, all the XRD peaks were refined in the framework of seven crystal system. The deviation between experimental and computational value of interplanar spacing (shown in Table 1) was found minimum ($\sigma = 0.024$) for tetragonal structure, which suggest the investigated sample crystallize in tetragonal structure. The lattice parameters obtain are $a = b = 7.804 \text{ \AA}$, $c = 20.751 \text{ \AA}$, $c/a = 2.6591$ and $V = 1263.81 (\text{\AA})^3$. As all the XRD peaks were index well for tetragonal structure with above unit cell parameters, it suggests formation of single phase compound. The appearance of strong intensity XRD peak with Miller index (2 2 0) along $2\theta = 32.3^0$ affirms majority of the crystal is growing along [2 2 0]. The observed slight broadening in the XRD profile was expected due to titling of the octahedral FeO₆ and TiO₆ from their ideal position. Further investigation on structural parameters, atomic positions, reliability factors were done by reitveld refinement technique using MATCH software (version 2.0). The refinement profile and detail atomic position obtained through reitveld technique is illustrated in Fig. 2 and Table 2 respectively. The observed least value of reduce (chi)² ($\chi^2 = 2.3$) and average Bragg R-factor ($R_B = 12.8 \%$) for tetragonal system (space group = P4bm) once again clarify that the investigated sample crystallize in tetragonal structure.

Table 1
Comparison of experimental and calculated d-spacing for different Bragg's planes.

Serial No.	Bragg's angle (θ)	d-spacing (experimental)	d-spacing (calculated)	$h \ k \ l$
1	22.77	3.9020	3.9020	2 0 0
2	26.93	3.3079	3.3079	2 1 2
3	32.37	2.7633	2.7591	2 2 0
4	39.89	2.2580	2.2594	2 1 7
5	43.57	2.0755	2.0752	0 0 10
6	46.45	1.9533	1.9553	3 0 7
7	52.37	1.7455	1.7450	4 2 0
8	57.81	1.5935	1.5953	4 1 7
9	63.41	1.4656	1.4653	2 2 12
10	67.89	1.3794	1.3796	4 4 0
11	72.53	1.3022	1.3019	5 2 7
12	77.17	1.2350	1.2354	4 0 13

The surface morphological investigation of the prepared sample $\text{Li}_2\text{LaFeTiO}_6$ was carried out on pellet sample at room temperature using scanning electron microscope (SEM) is shown in Fig. 3. The polycrystalline nature was reveal from the micrograph as it consists of grains of varying size and shape distributed non-uniformly throughout the pellet sample. Certain sort of clustering of grains observed in the micrograph may be due to high temperature sintering of the pellet sample. Even after sintering at high temperature, certain amounts of voids are noticed on close observation which can trigger the hopping conduction mechanism of charges [14]. Relatively high concentration of small grains in the micrograph was expected due to collapsing of large grains during the transport of oxygen ion vacancies through the grain boundaries. The average grain size was found $3.82 \mu\text{m}$ through intercept technique.

3.2. FTIR spectroscopy:

The investigation of different modes of vibration and functional groups present in the sample was done by FTIR spectroscopic technique as shown in Fig. 4. The FTIR spectra was found to consists of some characteristic bands located at around $453, 567, 876, 927, 1000, 1134, 1433, 1505$ and 3405 cm^{-1} . The perovskite based materials generally found to possess some characteristic band linked with lattice vibration in the range $850 - 400 \text{ cm}^{-1}$ [15]. The bands at 453 and 567 cm^{-1} assigned to stretching of Ti-O and Fe-O bonds. The observed bands in the range $876 - 1000 \text{ cm}^{-1}$ is ascribing to Fe-O-Fe asymmetric vibration. The vibration of Gd-O bonds attribute to the band at 1134 cm^{-1} [16]. The observed weak

intensity bands at 1433 and 1505 cm⁻¹ may be attributing to vibration of carbonate ion (CO₃²⁻) [17]. The absorption of OH⁻ radicals attribute to the band at 3405 cm⁻¹ in the investigated sample [17].

3.3. UV-Visible spectroscopy:

The opto-electric response of the prepared sample was investigated through UV-Visible spectroscopic technique. The absorbance and reflectance spectra of the investigated sample were depicted in Fig. 5. It was noticed from Fig. 5 (a) and Fig. 5 (c) that the response of the sample was relatively weak in the UV range whereas reverse trend was observed in Visible range. The absorbance cut-off of the sample was found nearly 650 nm which suggest the sample absorb visible radiation in the range 380–650 nm quite strongly. In order to calculate the energy bandgap (E_g) we have utilized the relation $(ahv)^{1/n} = A(hv - E_g)$ [18] proposed by Tauc, Mott and Davis. Where a = absorbance coefficient, v = frequency of incident radiation, A = proportionality constant & n = index ascribing different electronic transition. For n = 1/2, 3/2, 2 and 3, the transition is direct allowed, direct forbidden, indirect allowed and indirect forbidden respectively. In the present investigation we take n = 1/2 as perovskite materials generally undergoes direct allowed transition. The bandgap (E_g = 1.73 eV) of the material was extracted from the Tauc plot (Fig. 5 (b)) by extrapolating the tangent line on hv axis. Besides Tauc function, we have also utilized Kubelka-Munk function [19] F (R) = (1 - R)/2R (where R = reflectance coefficient) to calculate the bandgap from reflectance data. The estimated band gap (E_g = 1.87 eV) from the reflectance data was found comparable with the value obtained from absorbance data.

3.4. Dielectric spectroscopy:

The frequency dependent variation of relative permittivity/dielectric constant (ϵ_r) and loss tangent (tanδ) is depicted in Fig. 6 (a) and Fig. 6 (b) respectively. It was found that both the parameters ϵ_r and tanδ decreases with enhancement of frequency for all the selected temperatures. As per literature, the dielectric property of ceramic is very much influence by four kinds of polarizations, namely, electronic, ionic, dipolar/orientation and space charge polarization [20]. At low frequency, all the polarizations contribute significantly whereas at high frequency only electronic polarization attribute towards the total dielectric of the ceramic. The gradual disappearance of different polarizations with enhancement of frequency is the significant cause of dielectric dispersion in the investigated sample. The Maxwell-Wagner and Koop's phenomenological theory [21] was found quite consistent with the observed dielectric anomaly in the investigated sample. As per the theory, the ceramic dielectrics are consists of two types of layers (i) semiconducting grains and (ii) insulating grain boundaries. The grain boundaries are more prominent at low frequency region whereas the grains are more prominent at high frequency region. Due to insulating nature of grain boundaries, the charge carriers (like electrons) get accumulate on it which increases the trapped charge density and hence ϵ_r value. To move the charge carriers via grain boundaries, energy required is more and hence high tanδ value. On increasing the frequency, the density of trapped charges on grain boundaries keep on decrease and charges start to slide over the grain by dissipating less energy and hence ϵ_r and tanδ is also low.

Also it is noticed from Fig. 7 (a) and Fig. 7 (b) that the value of dielectric parameters ϵ_r and $\tan\delta$ almost attain saturation level below 350^0C and above it both of them start to rise sharply without encountering any transition (magnetic and/or ferroelectric) in the specified temperature range $25^0\text{C}-525^0\text{C}$. Such observation suggests the transition may be lie beyond the experimental constraint temperature. The asymptotic variation of ϵ_r and $\tan\delta$ above 350^0C may be assign to thermally activated hopping conduction in the system. As B-site of the investigated sample was occupied by Fe and Ti ion, it was expected that the creation of oxygen vacancies due to high temperature sintering can cause valence fluctuation ($\text{Fe}^{3+}\leftrightarrow\text{Fe}^{2+}$) and ($\text{Ti}^{4+}\leftrightarrow\text{Ti}^{3+}$) and enhancing the hopping conduction of charge carriers in the material. The other possibilities of high value of dielectric parameters at elevated temperature are (i) electron-phonon interaction at the lattice site (ii) presence of some imperfection/dislocation in the crystal and (iii) domination of conductivity.

3.5. Impedance study:

Non-destructive impedance spectroscopy method was adopted to study the influence of grains, grain boundaries and electrodes in the characterization of electrical properties. In this method, an electrical perturbation was induced in the dielectric system and its output response was recorded over varying range of frequency and temperature. In order to evaluating the resistive (Z') and reactive (Z'') components of complex impedance (Z^*), the following equations were utilized

$$Z^* = Z' + i Z''$$

$$Z' = R/(1 + \omega^2\tau^2)$$

$$Z'' = -\omega R^2 C / (1 + \omega^2\tau^2)$$

Where τ is the relaxation time and is define as $\tau = RC$.

The frequency-temperature dependent variation of resistive (Z') and reactive (Z'') is depicted in Fig. 8 (a) and Fig. 8 (b) respectively. From Z' versus frequency spectra, it was noticed that Z' value fall in a sigmoidal manner below 10 kHz which suggests the lowering in density of trapped charges at grain boundaries [22]. The overlapping of all the curves above 10 kHz irrespective of temperature signifies the release of space charges and domination of ac conductivity in the material at high frequency [23]. It is observed from Z'' versus frequency spectra, the value of Z'' raise proportionally with frequency and attain maxima at a characteristics frequency (commonly known as relaxation frequency) and then gradually fall and attain saturation in high frequency. The shifting of maxima peak in the direction of increasing frequency with enhancement of temperature suggests the relaxation in the material is temperature dependent and is non-Debye type [24]. The broadening of maxima peak in Z'' spectra with enhancement of temperature suggests spread of relaxation and fall of relaxation time in the investigated material. The low temperature relaxation in the material is ascribing to immobile charges and that at high temperature is due to oxygen vacancies and/or some intrinsic defect. The NTCR behavior in the material is also reflected from both Z' and Z'' spectra.

The change of Nyquist plots (i.e., Z'' vs Z') at various temperatures was depicted in Fig. 8 (c). The observed single semicircular arc in the Nyquist plot suggests the resistive and capacitive property was highly influence by the grains in the material. As per Debye hypothesis, an ideal semicircular arc with center lie on the Z' axis corresponds to single relaxation process and homogeneity in the material. The depressed semicircle with center lies below the Z' axis suggests the non-Debye type of relaxation and inhomogeneity in the investigated sample [25]. To correlate the electrical and microstructural properties, an equivalent circuit model consists of capacitor (C) and resistor (R) was incorporated. The experimental data were fitted with the theoretical ones using software ZSIMWIN (version 2.0). In order to counter the observed depression in the semicircular arc, a new element, namely constant phase element (CPE) Q was introduce in the RC network. It was noticed that the experimental data were fitted well for the equivalent circuit ($C \parallel Q \parallel R$) (insert in Fig. 8 (c)). Such observation suggests significant contribution of grains in the electrical and transport mechanism [26]. The slight deviation observed in the semicircular arc from the model generated curve at low frequency was might be due to weak contribution of grain boundaries.

3.6. Modulus study:

The complex modulus spectroscopic method is also incorporated in addition of impedance technique to have better understand of different processes such as (i) relaxation (ii) conduction (iii) transport etc. occurring in the investigated sample. The advantage with modulus technique is that it can extract the contribution of small capacitance in the material which sometimes gets suppressed in impedance technique due to inhomogeneous distribution of grains [27]. The real (M') and imaginary (M'') components of complex modulus (M^*) was extracted using the following equations

$$M^* = M' + i M''$$

$$M' = C_0/C [(\omega \tau)^2 / \{1 + (\omega \tau)^2\}]$$

$$M'' = C_0/C [(\omega \tau) / \{1 + (\omega \tau)^2\}]$$

Where C_0 is the geometrical capacitance and is define as $C_0 = \epsilon_0 A/d$ (ϵ_0 = permittivity of free space, A and d are respectively area and thickness of the circular pellet)

It is observed from the variation of M' versus frequency spectra (Fig. 9 (a)) that M' has negligibly small value in the low frequency region which suggest insignificant contribution of electrode polarization. The monotonic dispersion observed in M' spectra at intermediate frequency region attributes the short range mobility of charge carriers influence the conduction process. The mobility is due to the lack of restoring force of charge carriers in external electric perturbation. The merging of all curves irrespective of temperature ascribe to lack of space charges in high frequency region [28, 29].

From M'' versus frequency spectra (Fig. 9 (b)), it is found that M'' value increases with frequency and reach a maxima. The relaxation in the material is once again clarify from M'' spectra. The temperature dependent relaxation is observed from the shifting of relaxation peak towards high frequency which is

due to activation of hopping conduction through thermal agitation. The asymmetric broadening of M" spectra signifies non-Debye type of relaxation [30, 31].

In order to illustrate, the response of small capacitance and large resistance in the material, the relative variation of Z" and M" with frequency (Fig. 10 (a)) is studied at a particular temperature. It also enables to distinguish whether the relaxation in the material is dominated by short range or long range charge carriers. For long range process, Z" and M" relaxation peaks appear at nearly common frequency whereas for short range process, they appear at different frequencies. The observed mismatching of Z" and M" peaks in the investigated sample suggests short range charge carriers are dominating the relaxation mechanism [32, 33].

The relaxation time (τ) obtained from Z" and M" spectra is studied as a function of temperature as depicted in Fig. 10 (b). In order to estimate the value of τ we have utilized the relation $\tau = 1/2\pi f_r$, where f_r corresponds to frequency of relaxation. The observed values of τ are found to fit well with Arrhenius relation [34] $\tau = \tau_0 \exp(-E_a/K_B T)$, where E_a = activation energy. The $E_a = 1.109$ eV value estimated from Z" spectrum correspond to localized conduction while $E_a = 1.087$ eV obtained from M" spectrum correspond to delocalized conduction [33, 34]. The observed closeness of E_a value illustrates that similar sort of charge carriers are participated in both the conduction process.

3.7. AC conductivity study:

The frequency dependent variation of ac conductivity (σ_{ac}) at selected temperatures is depicted in Fig. 11 (a). It is noticed that the variation of σ_{ac} is relatively small in low frequency range whereas at high frequency it rises sharply. The observed dispersion in σ_{ac} spectra can be ascribed to the presence of space charges as well as disorderness of the cations at A-site and B-site [35]. The conductivity spectra was found very much consistent with Jonscher's power law $\sigma_{ac} = \sigma_0 + Aw^n$ [36]. As per the law, the origin of frequency dependent conductivity is related to the relaxation phenomenon of mobile charges. Also it is noticed that the slope of the ac conductivity spectra is relatively high at high frequency than that at low frequency region. Such observation suggests the hopping mechanism of charges is quite dominating in the conduction process. The presence of multi-valent ions Fe and Ti at B-site can initiate the hopping conduction of electron between ($Fe^{3+} \leftrightarrow Fe^{2+}$) and ($Ti^{4+} \leftrightarrow Ti^{3+}$) in the investigated sample.

The temperature dependent variation of σ_{ac} at selected frequencies is shown in Fig. 11 (b). The NTCR behaviour of the material was confirmed as σ_{ac} increases with temperature. The high value of σ_{ac} at high temperature region attributes to higher mobility of charges due to hopping between localised sites [37]. The activation energy (E_a) was calculated in high temperature region by fitting the Arrhenius equation $\sigma_{ac} = \sigma_0 \exp(-E_a/K_B T)$ in the experimental data. The obtained values of E_a were 1.027 eV, 0.791 eV, 0.475 eV, 0.329 eV and 0.295 eV at frequencies 1 kHz, 10 kHz, 100 kHz, 1 MHz and 5 MHz respectively. The E_a value was found high at low frequency than that of high frequency. With increase in frequency, the transportation of charge carriers between localized sites enhances and hence activation energy decreases.

Table 2: Detail atomic position of various elements in $\text{Li}_2\text{GdFeTiO}_6$ obtained through Rietveld refinement using MATCH software

Atom site	Atom type	X	Y	Z
Li 1	Li^+	0.5	0	0.5615
Gd 1	Gd^{3+}	0.5	0	0.5615
Fe 1	Fe^{3+}	0	0	0.0843
Ti 1	Ti^{4+}	0	0	0.0843
O 1	O^{2-}	0	0	0.4539
O 2	O^{2-}	0.2642	0.2357	-0.006

4. Conclusion

The XRD investigation on double perovskite $\text{Li}_2\text{GdFeTiO}_6$ synthesized through solid solution technique reveals formation of single phase new compound crystallize in tetragonal structure (space group = P4bm). The appearance of grains of varying size and shape with little amount of porosity in SEM morphology reveals formation of quite high density polycrystalline material. The perovskite phase and different vibrational modes in the sample was identified through FTIR spectroscopy. The narrow bandgap ($E_g = 1.73$ eV) and visible light sensitivity reveal through UV-Visible spectroscopy suggests the usefulness of the material for photovoltaic device. The room temperature dielectric parameters suggest it can be utilized for storage application. Conductivity, impedance and modulus techniques reveal the basic transport phenomenon in the material was influence by grains and grain boundaries.

References

1. Ryu, S. Priya, K. Uchino, H.E. Kim, J. Electroceram. **8** (2002) 107.
2. Turchenko, A. Trukhanov, S. Trukhanov, M. Balasoiu, N. Lupu, J. Magn. Magn. Mater. **477** (2019) 9–16.
3. O. Bohnke, Solid State Ionics, **179** (2008) 9.
4. Z. F. Zheng, H. Z. Fang, Z. K. Liu, and Y. Wang, J Electrochem Soc, **162** (2015) 244.
5. A. G. Belous, G. N. Novitskaya, S. V. Polyanetskaya, and Y. I. Gornikov, Inorg Mater, **23** (1987) 412.
6. Stramare, V. Thangadurai, and W. Weppner, Chem. Mater. **15** (2003) 3974.
7. Yoshinori, S. Shinichiro and N. Naoto Rep. Prog. Phys. **77** (2014) 076501
8. Sahoo, P. K. Mahapatra, R. N. P Choudhary, M. L Nandagoswami and A. Kumar, Mater. Res. Express **3** (2016) 065017

9. C. Sahoo, S. Das, T.K. Nath, Journal of Magnetism and Magnetic Materials, doi.org/10.1016/j.jmmm.2018.04.039
10. Kumar, G. Giovannetti, J. van den Brink, and S. Picozzi, Phys. Rev. B **82** (2010) 134429.
11. Yañez-Vilar, E. D. Mun, V. S. Zapf, B. G. Ueland, J. S. Gardner, J. D. Thompson, J. Singleton, M. M. Sánchez-Andujar, J. Mira, N. Biskup, M. A. Señaris-Rodríguez, and C. D. Batista, Phys. Rev. B **84** (2011) 134427.
12. J. Singh, and C. H. Park, Phys. Rev. Lett. **100** (2008) 087601.
13. B. M. Filho, A. P. Ayala, and C. W. de A. Paschoal, Appl. Phys. Lett. **102** (2013) 192902.
14. Wischnitzer, Introduction to Electron Microscopy, Pergamon Press, New York (1987).
15. Wischnitzer, Pergamon Press, New York (1987).
16. Andoulsi, K. Horchani-Naifer, M. Férid, Powder Technology **230** (2012) 183.
17. Bhaskar Kumar, S. Buddhudu, Ceramics International **35** (2009) 521.
18. P. Minutolo, G. Gambi, A. D'Alessio, Symposium (International) on Combustion 26 (1996) 951
19. Rai and A. K. Thakur , AIP Conference Proceedings **1728** (2016) 020491
20. J. Xie, Y. Akimune, K. Matsuo, T. Sugiyama, N. Hirosaki, T. Sekiya, Appl. Phys. Lett. **80** (2002) 835.
21. G. Koops, Phys. Rev. **83** (1951) 121
22. Rahmouni, M. Smari, B. Cherif, E. Dhahrib and K. Khirounia, Dalton Trans. **44** (2015) 10457.
23. Tilak, American Journal of Materials Science **2** (2012) 110.
24. Ranjan, R. Kumar, N. Kumar, B. Behera, R.N.P. Choudhary, J. Alloys Compd. **509** (2011) 6388–6394.
25. Sen, R.N.P. Choudhary, P. Pramanik, Electroceram. Phys. B **56** (2007) 387
26. Behera, P. Nayak, R.N.P. Choudhary, J. Alloys Comp. **436** (2007) 226.
27. G. McCrum, B.E. Read, G. Williams, Wiley, New York, 1967.
28. V.R. Chowdari, R. Gopalkrishnan, Solid State Ionics **23** (1987) 225.
29. C. Sutar, P. R. Das, R. N. P. Choudhary, Adv. Mat. Lett. **5** (2014) 131.
30. Pattanayak, B.N. Parida, P.R. Das, R.N.P. Choudhary, Appl.Phys. A **112** (2013) 387.
31. A.L. Nobre, S.J. Langfredi, Phys. Chem. Solids **62** (1999) 20.
32. C. Sinclair, A.R. West, J. Appl. Phys. **66** (1989) 3850.
33. K. Pradhan, R.N.P. Choudhary, C. Rinaldi, R.S. Katiyar, J.Appl. Phys. **106** (2009) 024102.
34. Zidi, A. Chaouchi, S d'astorg, M. Rguiti and C. Courtois, Bull. Mater. Sci., **38** (2015) 731–737.
35. N.K. Karan, D.K. Pradhan, R. Thomas, B. Natesan, R.S. Katiyar, Solid State Ionics 179 (2008) 689.
36. A.K. Jonscher, Nature 267 (1977) 673
37. A.E.F. Gabal, Y.M. Al Angari, A.Y. Obaid, ComptesRendusChimie **16** (2013) 704.

Figures

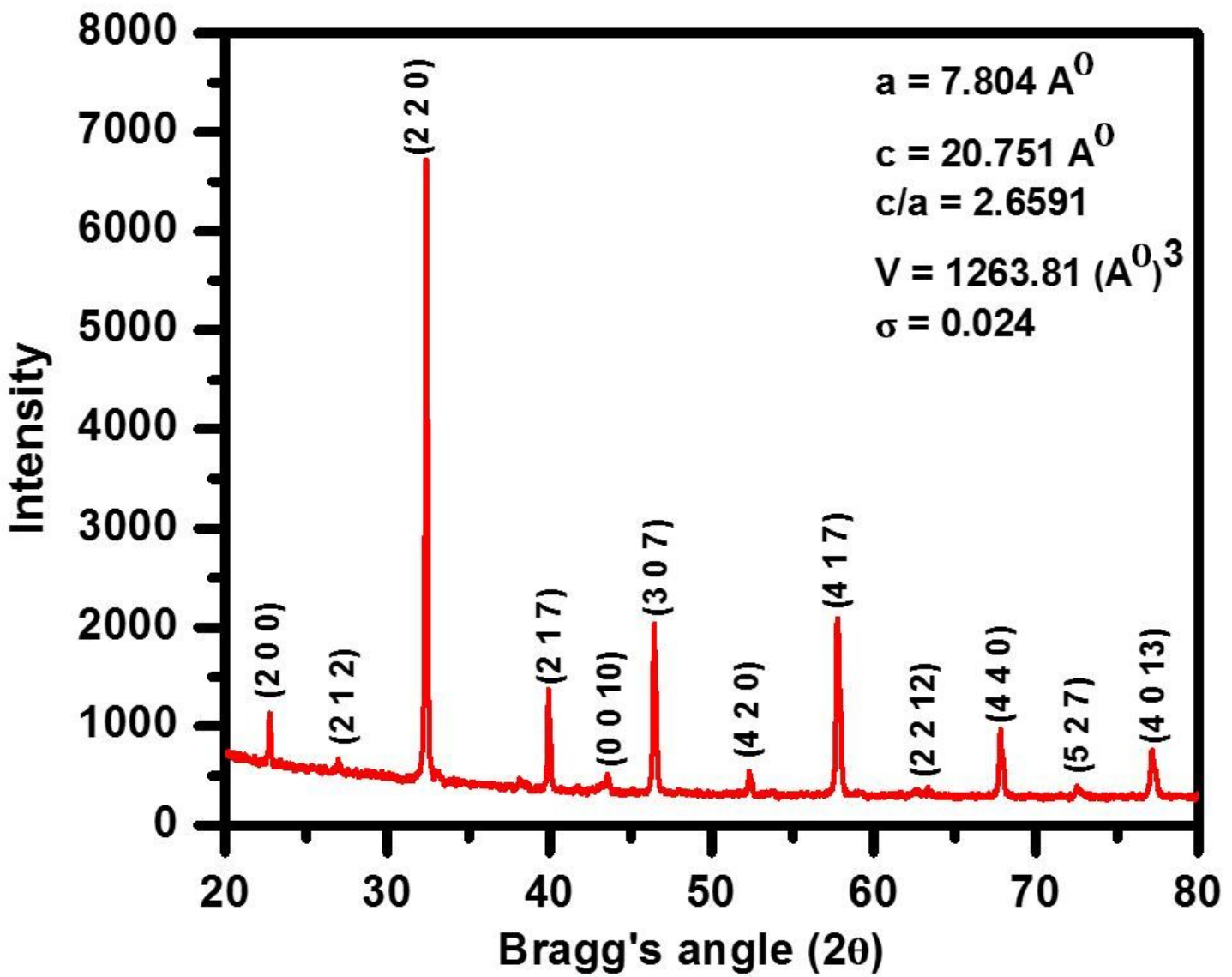


Figure 1

Exp. XRD profile with Bragg's indexing

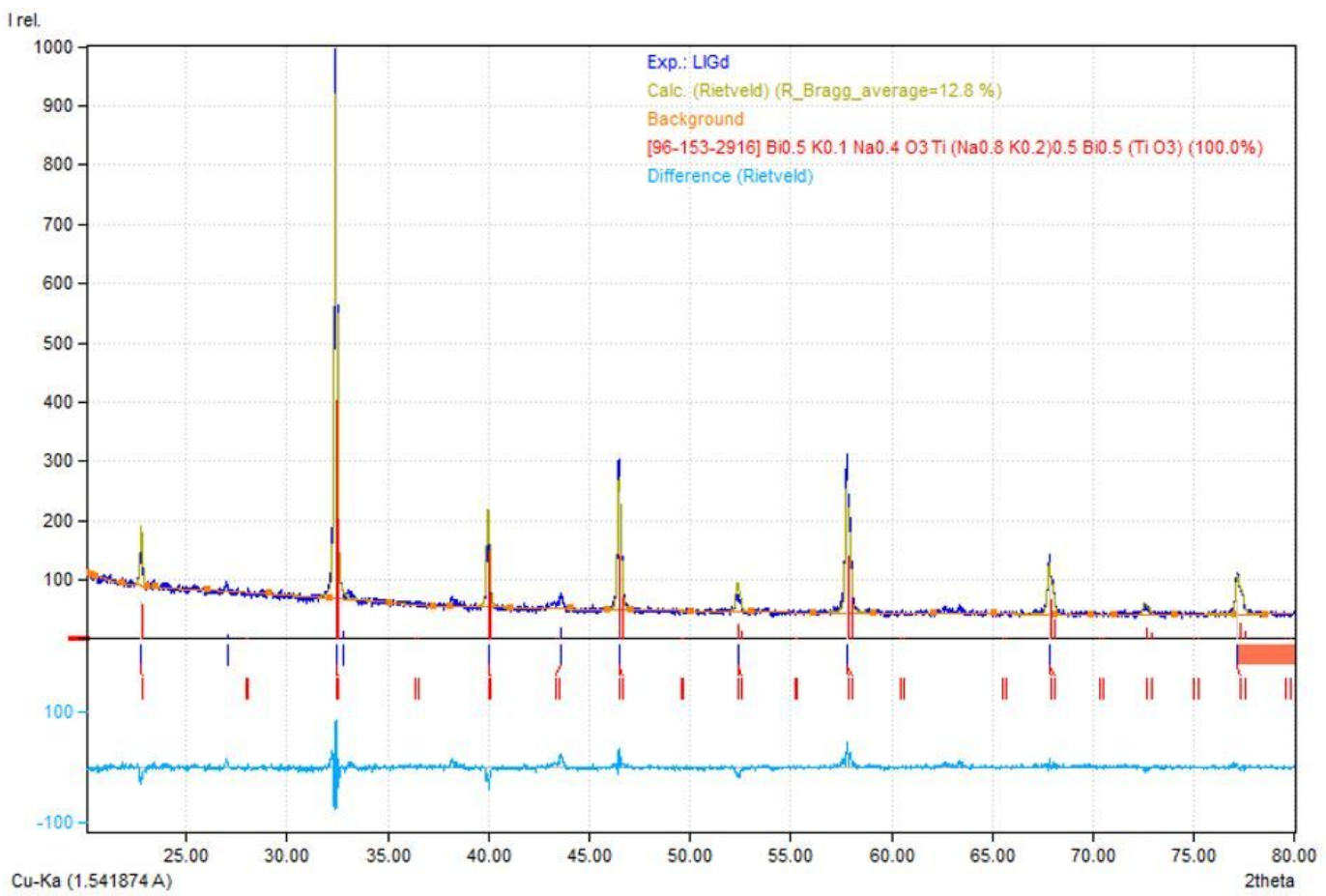
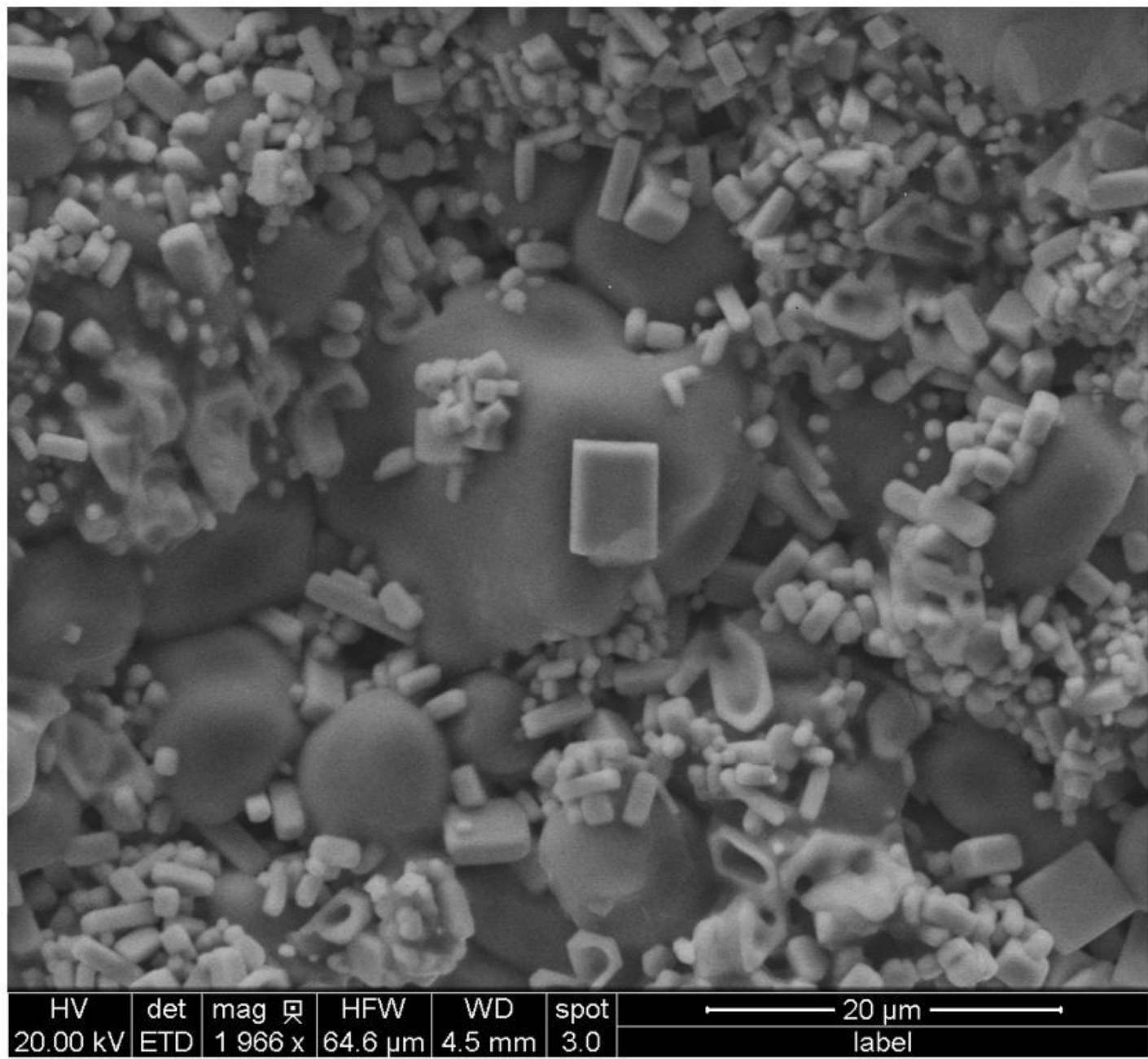


Figure 2

Rietveld refine XRD profile



HV	det	mag	RF	HFW	WD	spot	20 μm
20.00 kV	ETD	1 966 x		64.6 μm	4.5 mm	3.0	label

Figure 3

SEM morphology of the investigated sample

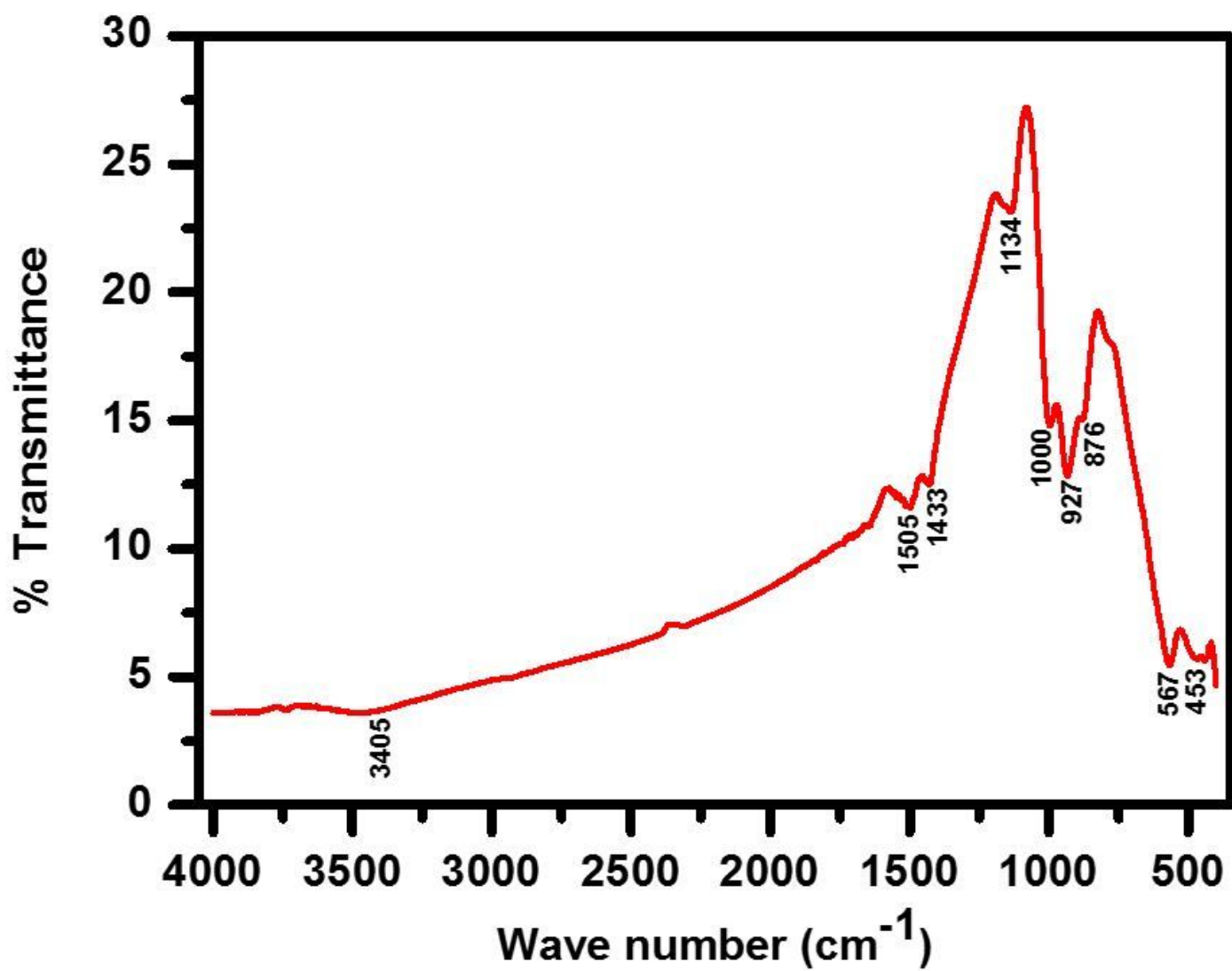


Figure 4

FTIR spectra of the prepared sample

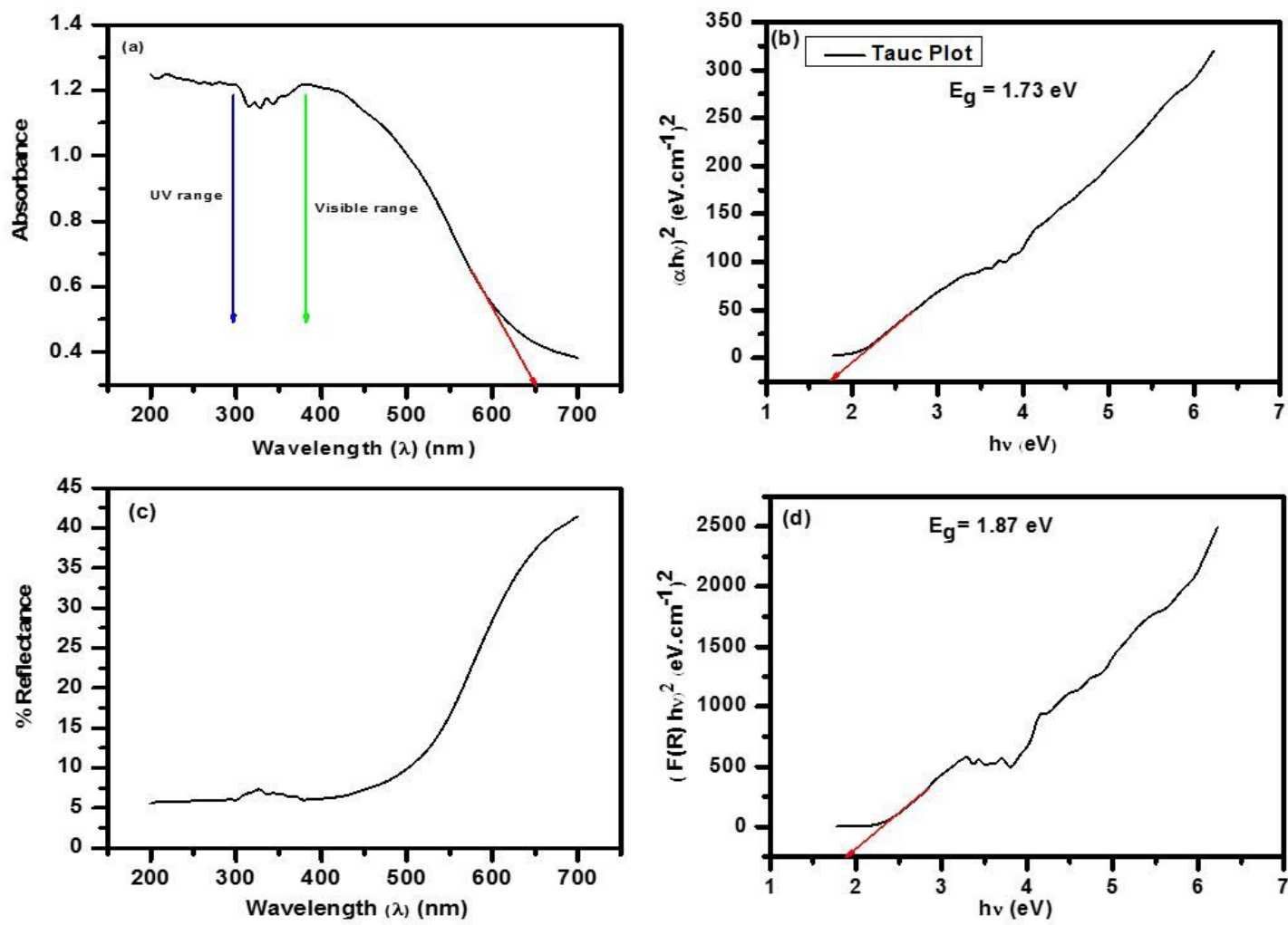


Figure 5

UV-Visible spectra of the prepared sample

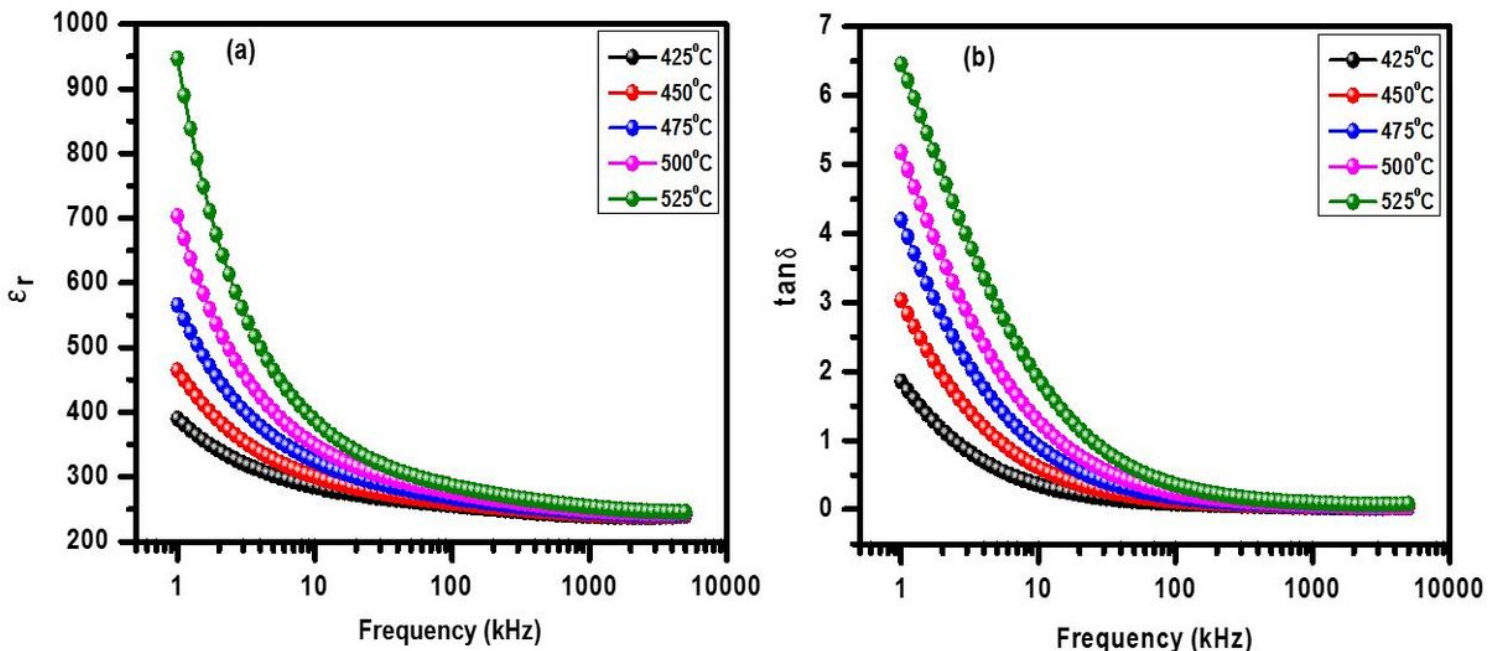


Figure 6

Frequency dependent dielectric spectra

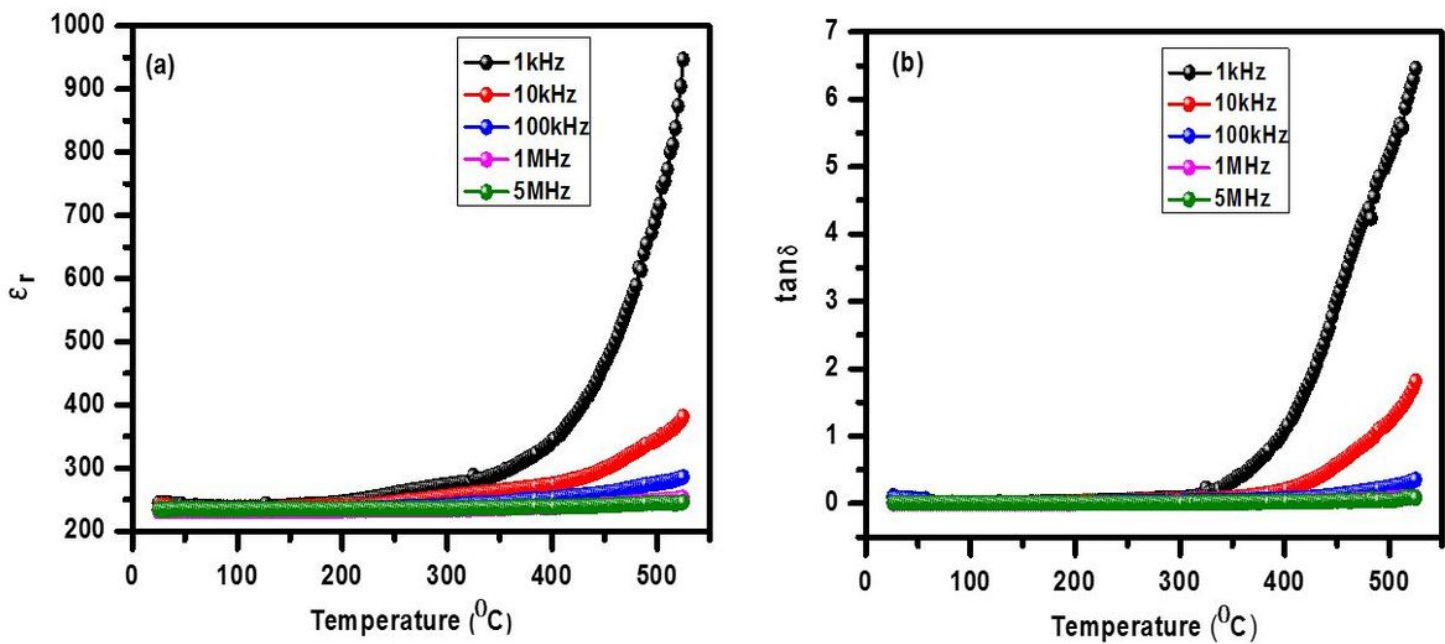


Figure 7

Temperature dependent dielectric spectra

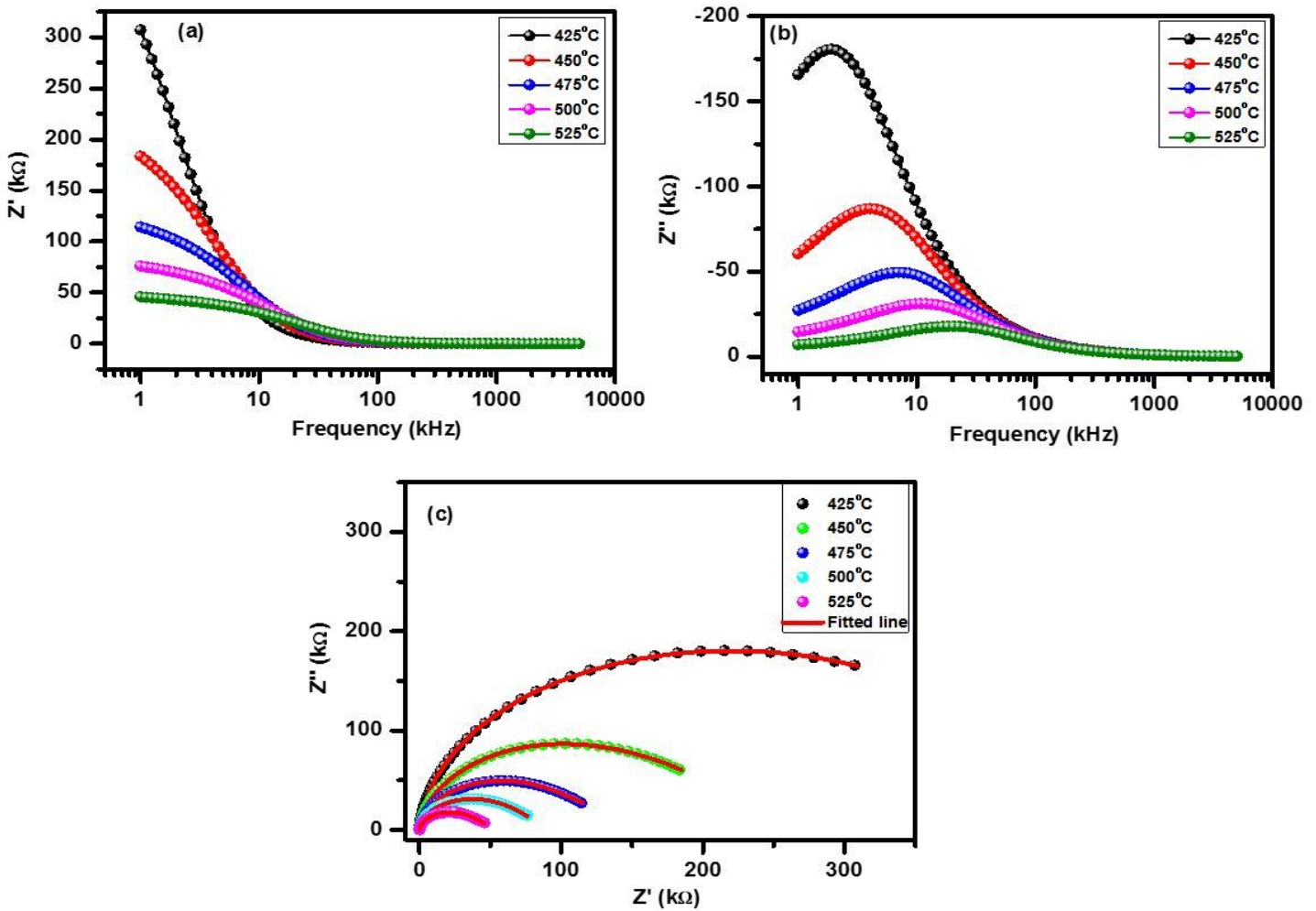


Figure 8

(a) Frequency dependent variation of Z' (b) Frequency dependent variation of Z'' (c) Nyquist plot

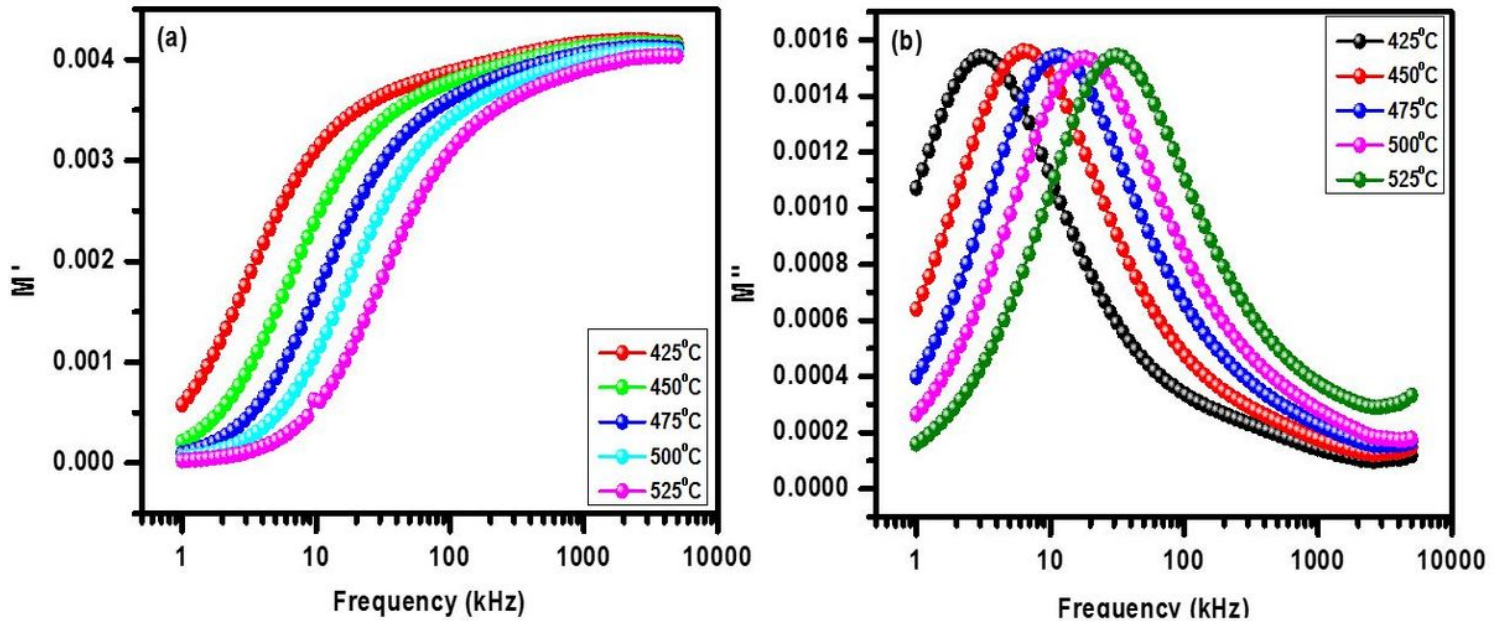


Figure 9

(a) Frequency dependent variation of M' (b) Frequency dependent variation of M''

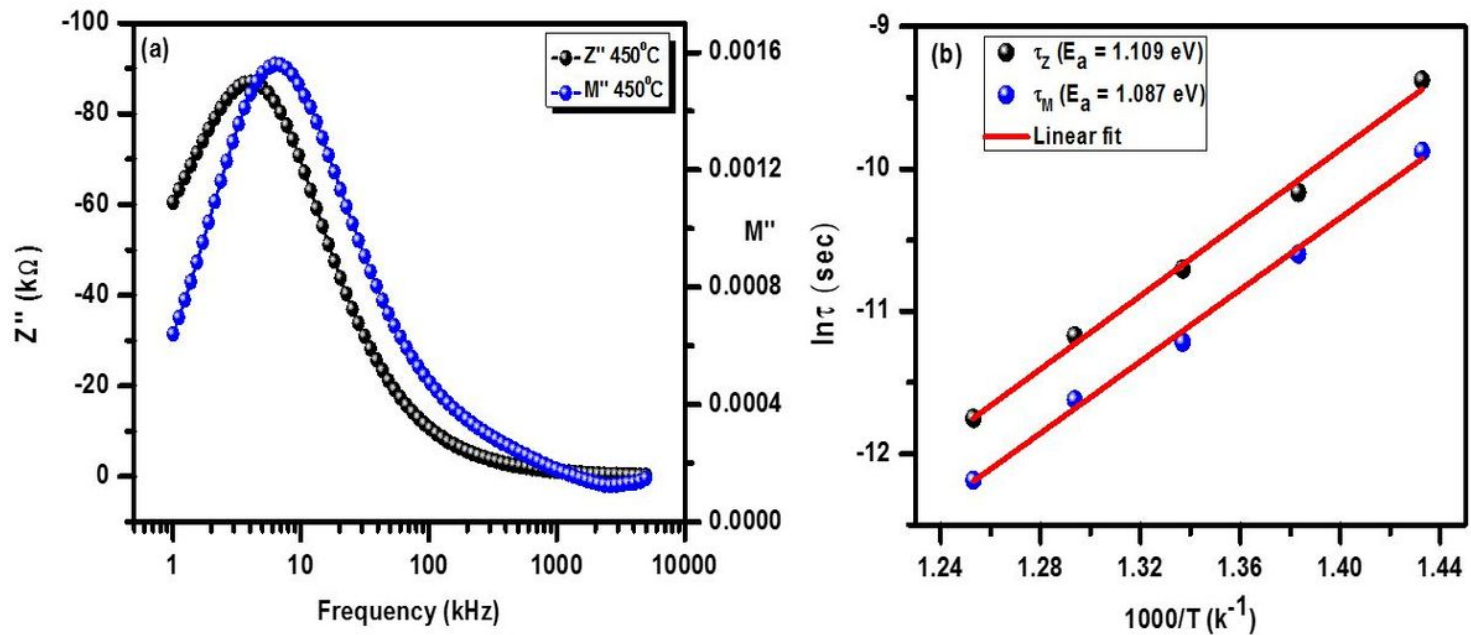


Figure 10

(a) Combine variation of Z'' & M'' with frequency (b) Variation of relaxation time with temperature

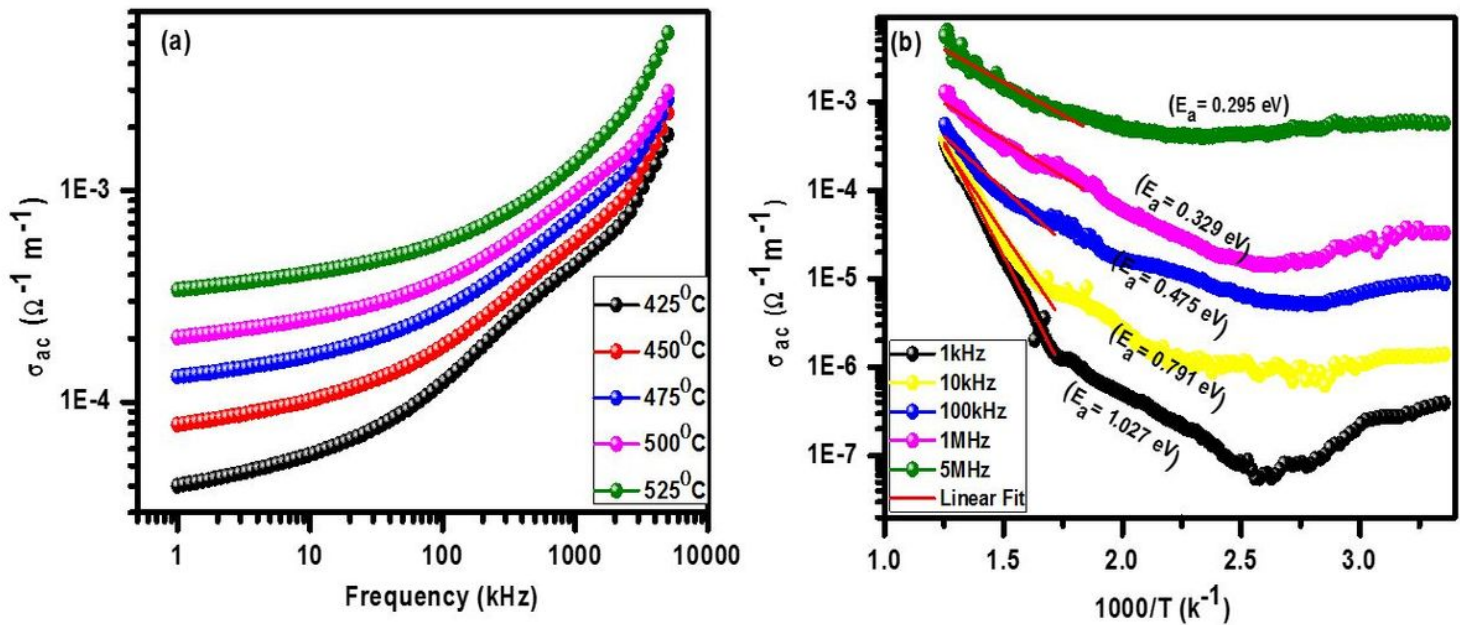


Figure 11

(a) Frequency dependent variation of σ_{ac} (b) Temperature dependent variation of σ_{ac}